Available online at www.sciencedirect.com

jmr&t Journal of Materials Research and Technology

journal homepage: www.elsevier.com/locate/jmrt

# Hot isostatic pressing and heat treatments of LPBFed $CoCuFeMnNiTi_{0.13}$ high-entropy alloy: microstructure and mechanical properties

J. Fiocchi [a,b], C.A. Biffi [a,*], M. Elnemr [b], J. Shipley [c], A. Tuissi [a], R. Casati [b,**]

[a] CNR ICMATE, National Research Council, Institute of Condensed Matter Chemistry and Technologies for Energy, Unit of Lecco, Via Previati 1/e, Lecco, 23900 Italy

[b] Department of Mechanical Engineering, Politecnico di Milano, Via La Masa 1, Milano, 20156 Italy

[c] Quintus Technologies AB, Quintusvägen 2, Västerås, 721 66 Sweden

ARTICLE INFO

*Article history:*
Received 8 May 2023
Accepted 21 September 2023
Available online 26 September 2023

*Keywords:*
High-entropy alloys
Laser powder bed fusion
Thermal treatment
Hot isostatic pressing
Microstructure
Mechanical behaviour

ABSTRACT

The present work explores the possibility of processing a $CoCuFeMnNiTi_{0.13}$ high-entropy alloy by laser powder bed fusion (LPBF). The alloy, produced under optimised processing conditions, presents good densification but also hot cracks, caused by the liquation of an inter-dendritic Cu-rich phase. Microstructure of the as-built alloy is characterised by face centred cubic (FCC) columnar grains, containing Cu-poor dendrites and Cu-rich inter-dendritic areas. The alloy, which was designed to be strengthened by spinodal decomposition and precipitation, was subjected to different thermo-mechanical treatments to try and improve its properties. Direct ageing and solution treatment and ageing produced a strong but brittle material (tensile strength of 683 MPa and elongation to failure of 1.3%), whereas hot isostatic pressing followed by controlled cooling was able to heal pores and cracks while triggering the desired microstructural transformations (spinodal decomposition and precipitation). This resulted into a balanced set of mechanical properties (tensile strength of 473 MPa and elongation to failure of 7.6%). This work shows that proper post-processing can mitigate the issues typically affecting LPBF fabricated HEAs, producing tailored microstructures with satisfactory mechanical performances.



## 1. Introduction

High-entropy alloys (HEAs) are a novel class of metallic materials [1], which are not based on the preponderant presence of a single element but rather on several components, which are able to promote the formation of solid solutions. At an early stage, HEAs were designed with equimolar concentration of alloying elements, but over the years studies have focused on alloys displaying more complex chemical compositions and microstructures, resulting in enhanced mechanical and functional properties. Such materials are more properly named complex concentrated alloys (CCAs) or multi-principal element alloys (MPEAs), though the term HEAs is still largely used.

As the knowledge of the basics of HEAs becomes more solid, growing attention is devoted to the investigation of the

* Corresponding author.
** Corresponding author.
E-mail addresses: carloalberto.biffi@cnr.it (C.A. Biffi), riccardo.casati@polimi.it (R. Casati).

https://doi.org/10.1016/j.jmrt.2023.09.223

effect of different processing methods on material properties. In particular, additive manufacturing (AM) is attracting considerable interest [2]: the coupling of the inherent advantages of AM processes (flexibility, reduced production of scrap material, ability of producing intricated and complex parts, refined microstructures and improved mechanical behaviour [3,4]) with those possibly offered by advanced materials such as HEAs (ample alloy design freedom, thermal stability, unprecedented mechanical properties) is extremely attractive. Moreover, owing to the presence of elements with largely different melting temperatures, the production of HEAs by conventional melting and casting route is affected by segregation phenomena and loss of low vapour pressure elements [5,6]: such issues may be overcome by the extremely rapid solidification condition ($10^5$–$10^7$ °C/s) typical of some AM processes process. For example, high cooling rates were found able to prevent the formation of ordered second phases and produce an homogeneous microstructure in an as-built $AlCrFe_2Ni_2$ medium-entropy alloy [7]. Laser powder bed fusion (LPBF) has been applied to numerous HEAs: the most studied ones are the Cantor alloy (CoCrFeMnNi) and its variant, the CoCrFeNi alloy, possibly modified by the addition of Al ($Al_x$CoCrFeNi, $Al_x$CoFeMnNi) and Cu (AlCoCrCuFeNi, AlCoCuFeNi, AlCrCuFeNi) [8]. Refractory HEAs containing V, W or Ti have also been explored [9]. CoCrFeMnNi alloy usually displayed good LPBF processability [10], although hot cracking was occasionally reported in some works [11]. Its microstructure in the as-built state was characterised by a cellular structure delimited by high-dislocation-density walls arranged in columns along the building direction and in a honeycomb-like fashion in the plane perpendicular to it [12]. Mn was shown to segregate along the cell walls and occasionally give rise to nanometric oxides, which contribute to the strength of the alloy through the Orowan mechanism [13]. The addition of Al in AlCoCrFeNi produced a shift of the solidification structure from FCC to BCC with extremely fine ordered B2 domains [14]; moreover, fluctuations of Cr concentrations, likely arising from a spinodal decomposition process, were reported. The processing of the alloy was also plagued by extensive cracking, which was attributed to the build-up of thermal stresses. Better results were obtained by decreasing the relative concentration of Al to obtain eutectic $AlCoCrFeNi_{2.1}$ [15] or $AlCrFe_2Ni_2$ [16] alloys, which attained good processability and improved mechanical resistance thanks to their dual-phase microstructure (FCC and BCC). Cu-containing alloys were found to be frequently affected by the formation of vertical microcracks propagating along high angle grain boundaries [17,18], but the amount of cracks could be reduced by increasing the amount of Ni in the alloy, which also allowed the transition from a columnar to an equiaxed grain structure [19]. Cu was shown to stabilize FCC crystal structure and to frequently segregate along grain boundaries.

As previously mentioned, significant processing faults, including porosities and cracks, affected most of the studied compositions, save the ones with high Ni content. In this light, the use of post-processing methods able to improve the characteristics of the LPBF processed alloy in terms of microstructure and defect content appears extremely interesting. In this respect, the traditional hot isostatic pressing (HIP) process has been successfully employed: it relies on simultaneously subjecting a component to high pressure and temperatures and was widely applied to reduce the number of closed porosities and heal cracks in several LPBF processed materials. As a consequence of such treatment, mechanical behaviour of LPBF processes HEAs can be strongly improved, mainly in terms of ductility [20]. Nevertheless, depending on the nature of the investigated alloy, HIP may also represent a critical step. Although its high-temperature holding is definitely useful in homogenizing the microstructure and dissolving second phases, the cooling step may prove problematic: harmful phases may precipitate during the cooling step if the cooling rate is not high enough, which is a common condition in conventional HIP (typical cooling rate is in the order of °C/min). For example, Joseph et al. observed the formation of σ phase in an $Al_{0.85}$CoCrFeNi alloy produced by direct laser fabrication and HIPed with a 5 °C/min cooling rate: such microstructural evolution resulted in a sharp loss in ductility during tensile testing [21]. Moreover, controlling the cooling rate after HIP may be instrumental in the view of successive ageing treatments, whose outcome may depend on the level of supersaturation attained during the post-HIP cooling [22].

The present paper deals with the LPBF processing of a $CoCuFeMnNiTi_{0.13}$ HEA. The system was proposed first by some of the present authors as a modification of the equiatomic CoCuFeMnNi alloy [23], itself deriving from the well-known Cantor alloy by substituting Cr with Cu [24]. In the conventionally produced alloy, the presence of Ti was found able to activate the formation of nanometric coherent $Ni_3Ti$ precipitates, which could effectively harden the alloy when properly aged. Moreover, ageing treatment leads to the spinodal decomposition of the solid solution, further contributing to the increase of material strength. Indeed, due to the miscibility gap of Cu with other alloying elements, the solid solution turns into a maze like structure, inducing a local modulations of lattice parameter and elastic properties of the matrix [23,25]. It may also be pointed out that the CoCuFeMnNi alloy, produced by casting and rolling, was successfully subjected to laser beam welding [26], giving rise to sound beads devoid of any defect. This result appears encouraging in the view of processing the similar $CoCuFeMnNiTi_{0.13}$ alloy by LPBF. Thus, this work aims at exploring the possibility of producing by LPBF a $CoCuFeMnNiTi_{0.13}$ alloy. Moreover, it will focus on post-processing treatments meant to exploit different second phase formation mechanisms to tailor the microstructure and the mechanical behaviour of the alloy: in this respect, conventional heat treatments and HIP will be addressed. The implementation of different post-HIP cooling speeds will be explored to assess the possibility of preventing second-phase formation during cooling and properly exploiting successive ageing treatments.

## 2. Materials and methods

$CoCuFeMnNiTi_{0.13}$ powder produced by gas atomization was used as feedstock for producing samples by LPBF as described in the following. Fig. 1a depicts a SEM picture of the powder, showing spherical shape and satellites onto the particles surface. Powder particles are characterised by $d_{50}$ of 31.6 μm,

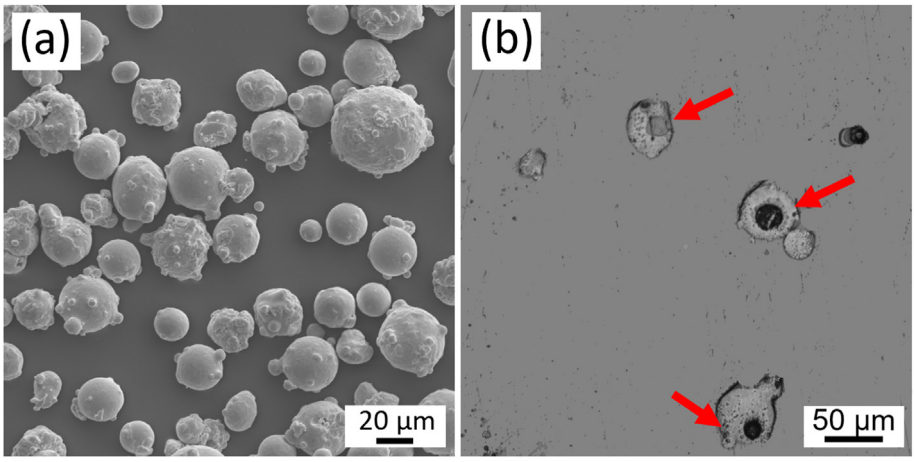


**Fig. 1 – (a) SEM micrograph showing the morphology of the used $CoCuFeMnNiTi_{0.13}$ powder; (b) optical micrograph showing the section of powder particles.**

with 80% of the particles lying in the 20–63 μm range. Metallographic sections revealed that a conspicuous fraction of the particles contain spherical porosities, likely deriving from gas entrapment taking place during atomization. Nominal and actual compositions of the feedstock are reported in Table 1.

The powder was processed by a Sharebot METALONE LPBF system, equipped with a 1 KW fiber laser and working under Ar atmosphere. Prismatic samples (5 × 5 × 10 $mm^3$ and 70 × 2 × 20 $mm^3$) were produced for density measurement, microstructure analysis, and mechanical characterisation. The main processing parameters are reported in Table 2. Subsize specimens for tensile testing, designed according to ASTM E8 standard, were obtained by electric discharge machining and showed an overall length of 70 mm and a thickness of 2 mm; the reduced section was 32 mm long and 4 mm large; the grip sections measured 10 mm × 16 mm.

Some of the samples were subjected to heat treatments and hot isostatic pressing (HIP). All heat treatments were carried out in muffle furnaces under Ar gas flow: solution treatment (1000 °C for 60 min) was followed by quenching in ambient temperature water; conversely ageing treatments (630 °C for durations ranging from 10 min to 360 min) was concluded by air cooling. HIP (mod. QIH by Quintus Technologies - Sweden) was performed at 1000 °C, with an Ar pressure of 150 MPa for 135 min, and was followed by two different cooling methods: a relatively fast cooling at 80 °C/min (hereafter named HIP-FC) and a proper quenching by gas jet at 5000 °C/min (hereafter named HIP-Q).

Density measurements were performed by means of Archimede's method on a Gibertini E50S2 precision digital balance. Morphological and microstructural analyses were carried out by optical microscope (Leitz Aristomet) and field emission scanning electron microscope (FE-SEM mod. Zeiss Sigma 500), equipped with energy-dispersive X-ray spectrometry (EDX) and electron backscatter diffraction (EBSD) detectors. Metallographic sections were finely polished down to 1 um cloth and etched with Nital 5% reagent. Structural analysis was performed by X-ray diffractometer (XRD, mod. Panalytical X'Pert Pro) equipped with Cu tube operating at 40 kV and 30 mA on the sections of the samples normal to the building direction in the 20°–120° 2θ range. Finally, mechanical properties were evaluated by micro-hardness tests (Future-Tech FM-810, applying a 300 gf load for 15 s) and tensile tests, which were performed by an MTS Exceed E45 universal testing machine at room temperature with a strain rate of 3.3 $10^{-4}$ $s^{-1}$.

**Table 2 – Constant and varied processing parameters used to process the $CoCuFeMnNiTi_{0.13}$ alloy.**

| Parameter | Value |
|---|---|
| Power | 100–400 W |
| Scanning speed | 300–800 mm/s |
| Scanning strategy | Meander |
| Atmosphere | Argon |
| Layer thickness | 50 μm |
| Hatch distance | 80 μm |
| Laser spot size | 65 μm |
| Building plate | Steel |

## 3. Results and discussion

### 3.1. *Process optimisation*

Laser power and scanning speed were varied according to a full factorial design (Table 2) to obtain almost fully-dense parts. The results of the feasibility study are reported in Fig. 2 in terms of material density vs. energy density. The trend is characterised by a steep increase of density for low

**Table 1 – Nominal and measured (EDX) chemical compositions (at.%) of the $CoCuFeMnNiTi_{0.13}$ powder.**

| | Co | Cu | Fe | Mn | Ni | Ti |
|---|---|---|---|---|---|---|
| **Nominal** | 19.5 | 19.5 | 19.5 | 19.5 | 19.5 | 2.5 |
| **Measured (EDX)** | 19.3 ± 0.3 | 19.0 ± 0.6 | 19.6 ± 0.4 | 20.0 ± 0.4 | 19.4 ± 0.5 | 2.6 ± 0.3 |

energy density values, followed by a maximum, and a softer decay. Such trend is typical of several LPBF fabricated alloys, and it is related to the mechanisms leading to the formation of different types of defects under different input energy conditions. In fact, lack of fusion defects presenting an irregular morphology were found in samples produced with energy density values up to 109 J/mm$^3$ (e.g., Fig. 1 b). On the contrary, when energy in excess of 147 J/mm$^3$ was delivered to the powder bed, a huge amount of large, spherical pores formed because of gas entrapment and local vaporization (Fig. 2 c), leading to an evident decrease of relative density. To a lower extent, spherical pores were also found in samples processed at lower energy densities, suggesting that the gas already present in the powder (Fig. 1) could not be evacuated during the process. The highest density (7,91 g/cm$^3$) was obtained by a laser power of 200 W and a scanning speed of 425 mm/s, corresponding to an energy density of 117.7 J/mm$^3$.

It shall be underlined that a considerable number of vertically oriented cracks was frequently found, independently from the specific processing condition. Cracks in materials fabricated using LPBF may be classified as cold or hot crack, according to their origin. Cold cracks arise in the solidified material because of the accumulation of internal strain deriving from thermal cycling. Hot cracks are related to melting and solidification phaenomena and they can be classified as solidification cracks or liquation cracks [27]. Solidification cracks occur in semi-solid metal during the final steps of solidification because of thermal contraction, and usually develop along grain boundaries. Liquation cracks, which are also intergranular, occur because of incipient melting of low-melting phases. Such liquation can be triggered by the heat propagating from melt pools laying on top of previously solidified layers. In the present work, cracks were found to cross several stacked melt pools, and to preferentially propagate along relatively thick inter-dendritic regions (Fig. 2 d and e), which, as it will be later discussed, were found to be rich in Cu. Moreover, crack path was sometimes observed to deviate from linearity, intersecting nearby gas porosities. The crack inner surfaces, shown in Fig. 2 f, reveal a dendritic structure, thus confirming the role of liquid phase in crack formation. In this respect, it is worth mentioning that a similar CoCuFeMnNi alloy, produced by rolling and homogenisation, did not exhibit cracks when subjected to laser welding [26]; on the contrary, an arc-meted AlCoCrCuFeNi alloy, processed by gas tungsten arc welding, presented extensive cracking in the HAZ, which was attributed to the early melting of the re-heated Cu-rich inter-dendritic phase characterising the ingot microstructure [28]. It is therefore reasonable to expect

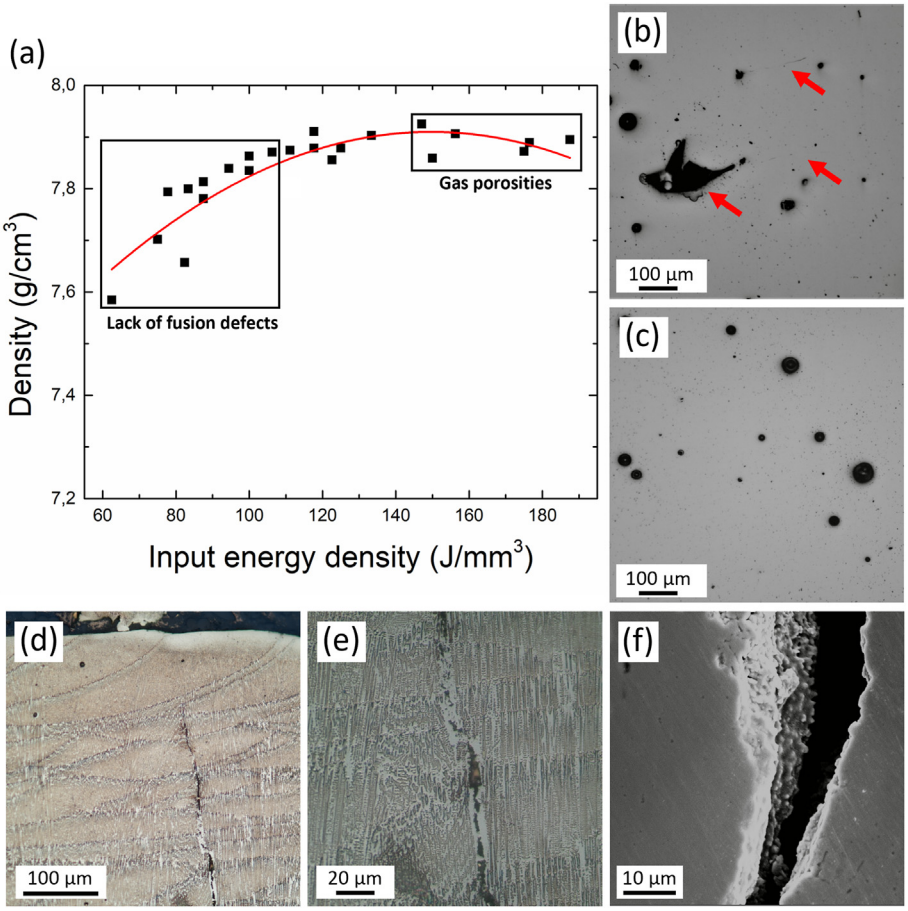


**Fig. 2 – (a) Density of LPBFed samples as a function of energy density; optical micrographs depicting the XZ sections of samples built with low (75 J/mm$^3$) (b), and excessive (175 J/mm$^3$) (c) energy density; optical (d, e) and SEM (f) micrographs depicting hot cracks propagating along the vertical direction in as-built samples.**

that repeated re-heating of the material and the fact that the re-heated material presents a dendritic structure characterised by Cu-rich inter-dendritic phase are necessary conditions for the development of cracks. Similar conditions apply for the LPBF process, due to its layer-by-layer nature, thus it is reasonable to conclude that a liquation-based mechanism may have caused the formation of cracks. This hypothesis is further enforced by the absence of cracks in the last layers on top of the sample, as well as by the fact that crack paths could be deviated by seemingly pre-existing pores. However it is also worth recalling that the dendritic structure of crack surfaces was reported to be a distinctive feature of solidification cracks [29]: indeed, discriminating between solidification and liquation cracks in a LPBFed part is not trivial [30].

### 3.2. *Microstructure of as-built parts*

The microstructure of as-built parts, reported in Fig. 3, can be described at several scales. As many other materials produced by LPBF, the alloy consists of the stacking of semi-cylindrical melt pools, which are about 150 μm wide and 60 μm deep, and can be distinguished thanks to the coarsening of the microstructure taking place along the melt pool borders (Fig. 3a and b; Figure S1 a). At a smaller scale, the solidification appears to be dendritic, with Fe- and Co-rich dendrites and Cu-rich inter-dendritic areas (Fig. 3 b, d). Such phase separation corresponds to the appearance of two sets of closely overlapped FCC peaks in the diffraction pattern reported in Fig. 3 e. The higher intensity peaks, likely referring to the primary phase (dendrites), are characterised by a lattice

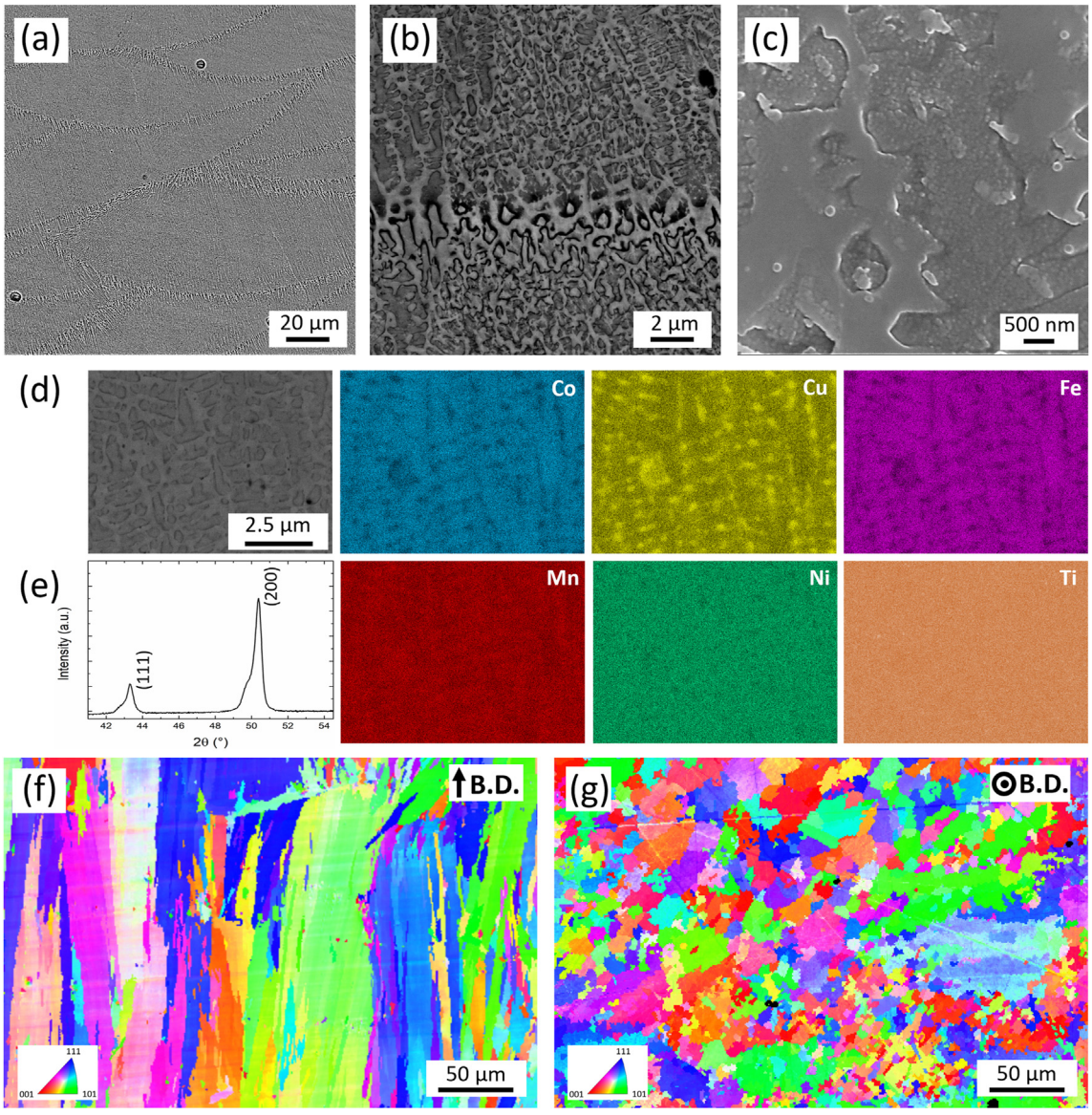


**Fig. 3 – Microstructure of as-built $CoCuFeMnNiTi_{0.13}$ alloy. FE-SEM micrographs depicting the melt-pool stacking (a) and the dendritic structure at low (b) and high magnification (c); EDS maps showing the elemental distribution inside melt pools (d); XRD pattern collected on the XY surface (e); IPF maps depicting the XZ section, parallel to the building direction (f), and XY section, normal to the building direction (g).**

parameter $d_{(111)} = 3.620 \pm 0.002$ Å, while the lower-angle set of reflections presents a $d_{(111)} = 3.649 \pm 0.009$ Å: such increment of the interatomic spacing is due to the local enrichment in Cu, which is the largest among the considered atoms, and is consistent with that reported in ref. [26] for a laser beam welded CoCuFeMnNi alloy displaying a similar microstructure. At a lower scale, inter-dendritic areas appear fairly uniform, whereas dendrites display evident contrast variations at their interior (Fig. 3 c). Indeed, a nanometric globular structure is noticeable, which is extremely similar to that observed at the interior of grains in the same $CoCuFeMnNiTi_{0.13}$ alloy produced by rolling and subjected to a solution treatment at 1000 °C [23]. Such microstructural features were described in ref. [20] as Cu-rich clusters, about 10 nm in diameter and coherent with respect to the surrounding matrix. They were also suggested to result from a spinodal decomposition process, likely taking place during quenching after solution treatment or, in the present case, during cooling of the just solidified material.

As expected, EBSD analysis (Fig. 3 f and g) revealed that the melt pools consist of columnar grains with longitudinal axis parallel to the building direction and extending through several melt pools. Such elongated grains present an average major axis of 77.4 μm and an average diameter of 13.8 μm in the XY section, i.e. the one transversal to the building direction. As a consequence the grain structure present a relatively high average aspect ratio close to 6. Despite such elongated appearance of the grains, it should be noted that the analysis of the corresponding IPF maps indicates that almost no texture exists along the building (Z) direction, thus suggesting that no epitaxial growth took place during the solidification of successive layers. The average grain orientation spread (GOS) value was found to be close to 1.3°, indicating a low misorientation within the grains [31].

### 3.3. *Heat treatment of the LPBF fabricated $CoCuFeMnNiTi_{0.13}$ alloy*

As mentioned in Section 1, the $CoCuFeMnNiTi_{0.13}$ alloy was specifically designed to be strengthened by second phases arising from spinodal decomposition and precipitation hardening. To promote a controlled formation of second phases, solution treatment followed by artificial ageing was applied to the conventionally produced alloy, leading to a considerable increase in strength [23]. Moreover, it is well-known that the rapid solidification involved in LPBF can produce supersaturated solid solutions (SSSSs), opening new opportunities to perform direct ageing treatment [32]. The effect of solution treatment and ageing and of direct ageing schedules was compared in terms of achievable hardness and tensile properties.

Fig. 4 shows the results of the ageing tests as well as of the microstructural analysis on the heat treated $CoCuFeMnNiTi_{0.13}$ alloy. The as-built and solution-treated conditions, display different hardness values, i.e., 221.9 ± 9.5 HV and 159.8 ± 10.4 HV, respectively. Nevertheless, the response of both as-built

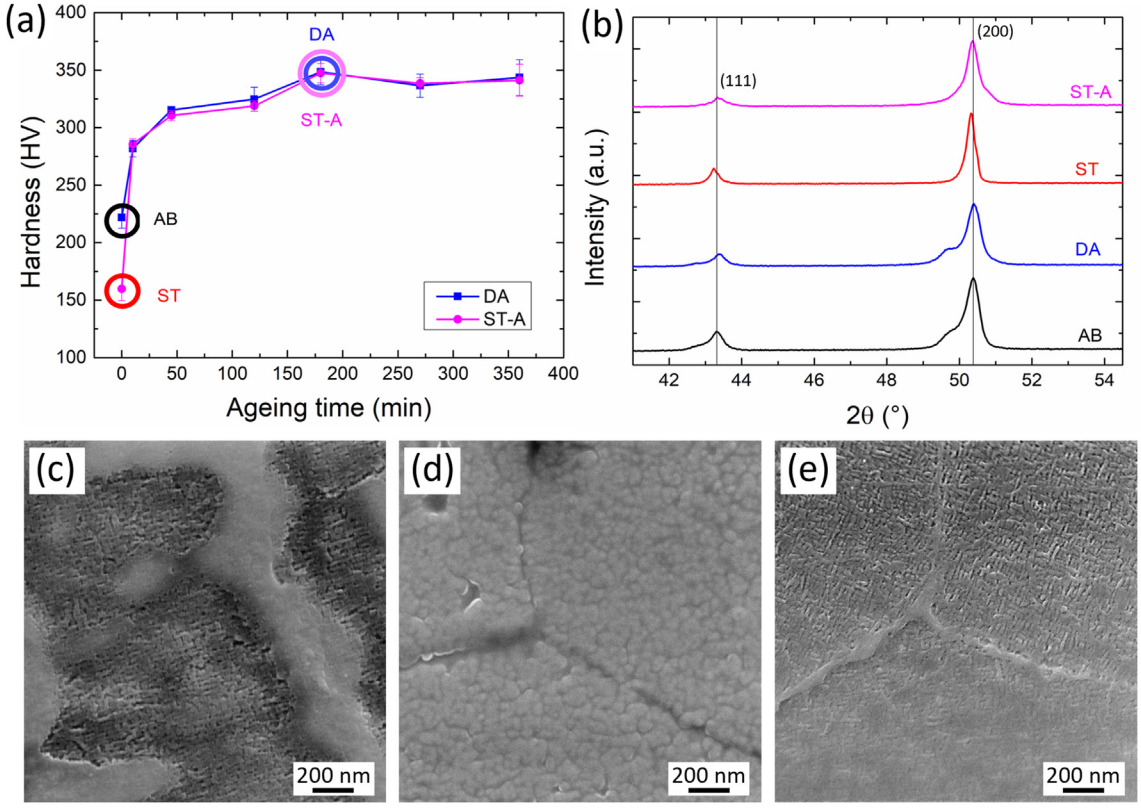


**Fig. 4 – (a) Ageing curves collected at 630 °C from the as-built and solution-treated conditions; (b) XRD patterns of as-built and heat treated conditions (magnified views of 41°–55° showing (111) and (200) reflections); FE-SEM micrographs of the $CoCuFeMnNiTi_{0.13}$ alloy in DA (c), ST (d) and ST-A (e) conditions.**

and solution treated parts to ageing treatment at 630 °C was similar, and the hardness gap was readily bridged after 10 min. After a steep hardness gain in the first 45 min, a maximum of about 350 HV is achieved after 3 h, regardless of the starting condition. Finally, a plateau is attained, and hardness remains almost constant, at least up to 6 h. SEM and XRD analyses were conducted on directly aged (DA, aged at 630 °C for 3 h), solution-treated (ST, annealed at 1000 °C for 1 h and quenched), solution treated and aged (ST-A, annealed at 1000 °C for 1 h, quenched and aged at 630 °C for 3 h) samples to investigate microstructure properties leading to the observed hardness trends.

The solution treatment (Fig. 4 d) dissolved the dendritic structure, which was observed in as-built samples, but was not able to induce a proper recrystallisation process. As may be appreciated by comparing Figure S1 c and the IPF map in Fig. 3 f, the original grain structure was not modified and ST samples presented uniform, elongated grains with average width of 12.6 μm (in the XY section) and length of about 71.3 μm (along the building direction). A limited Cu-enrichment was occasionally found along grain boundaries (up to 29.5 at.%, as evidenced by local EDX measurements), whereas the interior of grains was characterised by the same globular structures observed within the dendrites. Accordingly, the related XRD diffractogram displays one single set of FCC reflections with lattice parameter $d_{(111)} = 3.626 \pm 0.001$ Å. The increment of cell parameter with respect to that of the dendrites reflects the enrichment in Cu deriving from the dissolution of the dendritic structure. At the nanometric scale, the microstructural evolution induced by ageing is quite similar in DA and ST-A samples (Fig. 4 c, e). Ageing treatment was able to induce the formation of a maze-like structure in both conditions, i.e., Cu-rich discs that are coherent to the surrounding matrix and ordinately lye on its (100) planes. They result from the periodic modulation of Cu, Fe and Co concentration, which supposedly arises from a spinodal decomposition process [23]. The difference in lattice parameter between discs and matrix cannot be detected by the laboratory XRD equipment used in the present work; nevertheless, a slight broadening of the peaks related to ST-A and DA samples may be noticed in Fig. 4 b, in particular with respect to the ST condition. In DA samples (Fig. 4 c), the spinodal decomposition process leading to the formation of the maze-like structure took place in the inter-dendritic area only, which fits well with what described in the as-built condition. A Cu-rich second phase was also found to decorate the grain boundaries of ST-A samples. As the measured hardness increment is close to the one induced by ageing in the conventional alloy, it may be rightfully speculated that similar phases contribute to the observed strengthening. Therefore, besides the previously described Cu-rich phases constituting the maze-like structure, the presence of nanometric, coherent $L1_2$ $Ni_3Ti$ precipitates can be inferred, as reported in [23,25]. Cu-rich discs, resulting from spinodal decomposition, create a periodic compositional modulation, which causes a periodic modulation of both elastic properties and lattice parameter; concurrently, $Ni_3Ti$ $L1_2$ coherent nanoparticles are expected to give rise to discontinuous, localised and very intense peaks in elastic properties and shallower rises of lattice parameter. As a result, dislocation motion is expected to be opposed at long range through the continuous modulation of local lattice strain and elastic properties [23,33].

The observed hardening, as well as the related microstructural evolution, are extremely close to those observed in the conventionally produced counterpart. Indeed, the spinodal decomposition process is probably not affected to a great extent by the peculiarities of the LPBF process. Indeed, spinodal decomposition takes place through short-range diffusion and does not involve a nucleation step: as a consequence the presence of lattice defects (e.g. vacancies and dislocations, which could affect long-range diffusion [34]) has likely a negligible effect on it. On the contrary, residual stresses and dislocation accumulation, which are other well-known consequences of the LPBF process [12], would be expected to affect said processes: theoretical studies, as well as experimental evidence, indicate that spinodal decomposition has to overcome a higher energy barrier in crystalline solids than in liquids or glasses because of the presence of coherency stresses arising from the variation of lattice parameter with composition [35]. Therefore, if residual stresses can counterbalance said coherency stresses, they may be able to reduce the difference between coherent spinodal and chemical spinodal surfaces (see Section 2.3.2) and ease the decomposition of the solid solution. In this respect, the stress field associated to dislocation has been reported to accelerate the kinetics of spinodal decomposition in Fe–Cr alloys [36] and thin films [37]. However, it is very likely that this difference is considerable only in the very early stages of spinodal decomposition and that it progressively fades as the transformation reaches later stages.

### 3.4. *Hot isostatic pressing of the LPBFed $CoCuFeMnNiTi_{0.13}$ alloy*

In order to alleviate the issues deriving from pores and hot cracks, as-built samples were subjected to HIP at 1000 °C (i.e., the same temperature of solution treatment). Two batches of samples were subjected to different cooling rates after soaking, i.e., a fast cooling at 80 °C/min (HIP-FC) and a quench at 5000 °C/min (HIP-Q). HIP treatment was very effective in reducing the defect content, as shown by the results collected in Fig. 5. Indeed, both gas porosities and hot cracks were mostly closed, with only some of them remaining visible after the treatment. As result, the relative density was much improved from 94.04% density of the as-built sample to 99.78% and 99.77% of the HIP-FC and HIP-Q samples, respectively. It is also important to notice that the dispersion of the density data was significantly reduced by the HIP treatments.

The response of HIP-FC and HIP-Q samples to ageing was explored, yielding the hardening curves reported in Fig. 5 e. The microstructures of as-HIPed and HIPed and aged samples are shown in Fig. 5f–i. The relatively low cooling speed characterising the HIP-FC process was unable to avoid atomic rearrangement at the end of the HIP treatment: the resulting microstructure is indeed characterised by a maze-like structure, similar to that observed in the previously described DA ST-A samples. On the contrary, the spinodal decomposition process could not reach the same extent in HIP-Q samples, suggesting that the high cooling speed was able to prevent the

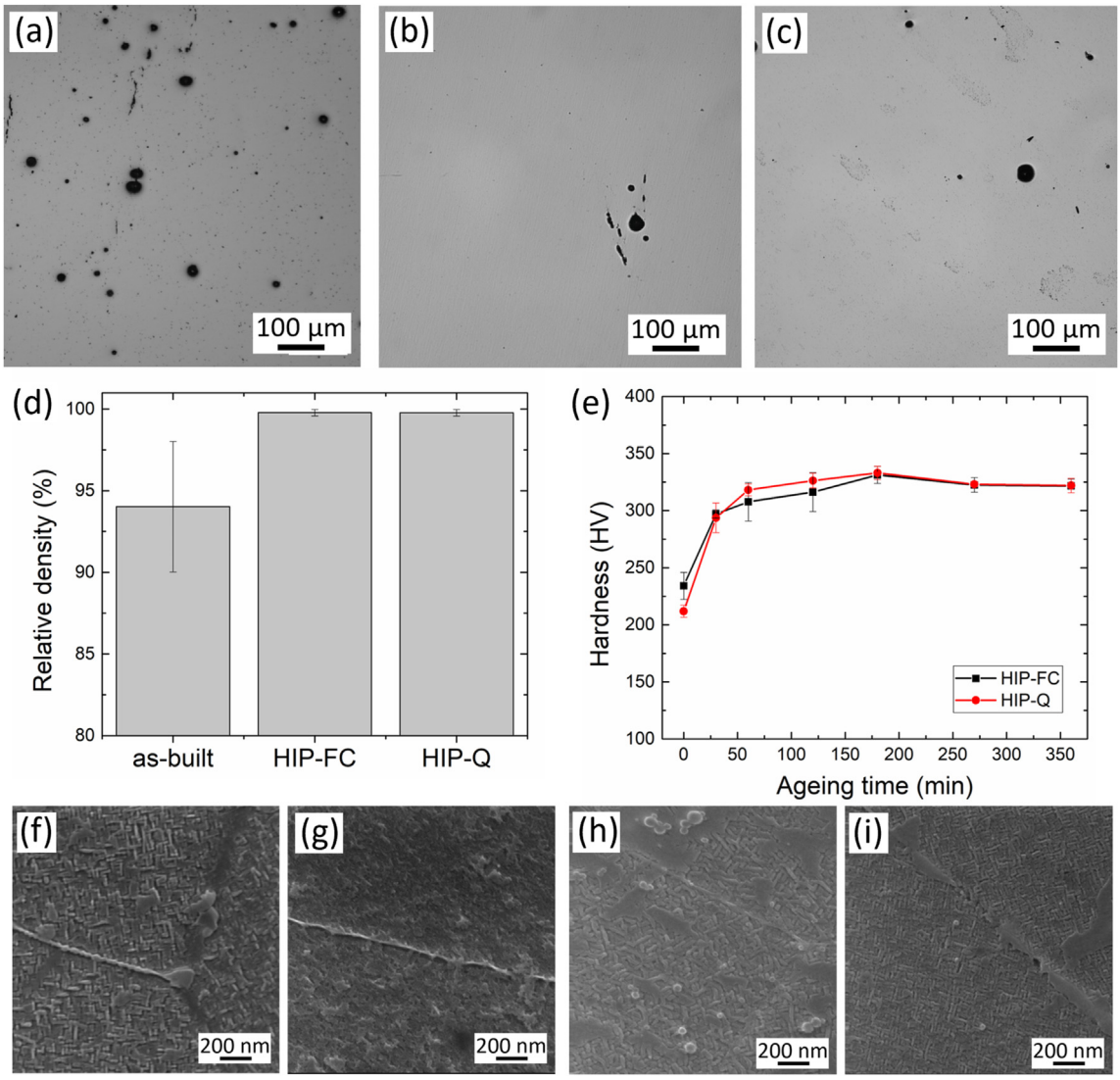


**Fig. 5 – Optical micrographs displaying internal defects in as-built (a), HIP-FC (b) and HIP-Q (c) samples; bar chart showing the resulting relative densities (d); ageing curves collected at 630 °C for HIP-Q and HIP-FC samples (e); FE-SEM micrographs depicting the microstructure of HIP-FC (f), HIP-Q (g), HIP-FC-aged (h) and HIP-Q-aged (i) samples.**

spinodal decomposition. As a consequence, HIP-Q samples had lower hardness (212 HV) than HIP-FC samples (234 HV). HIPed samples, regardless of the cooling speed, presented a Cu-rich phase at grain boundary. The following ageing treatment at 630 °C was able to induce hardening in both Q and FC conditions, leading to a maximum hardness of about 330 HV. If this trend is compared to that of ST-A and DA alloys, it may be appreciated that the timeframe for hardening is the same, as similar maximum hardness values are obtained after 3 h. Such comparison further confirms that both the strengthening mechanisms are insensitive to the starting condition of the material and result in fairly constant hardening with similar kinetics. Accordingly, the peak-aged samples (Fig. 5h and i) display microstructures, which are virtually indistinguishable from each other and from the ST-A and DA ones. In both conditions the maze-like structure resulting from Cu modulation is clearly recognizable and the Cu-rich second phase decorates grain boundaries.

### 3.5. *Mechanical behaviour*

The mechanical behaviour of the $CoCuFeMnNiTi_{0.13}$ alloy produced by LPBF was studied by tensile tests, yielding the results shown in Fig. 6. In the as-built condition the alloy was characterised by a yield strength of 410 ± 26 MPa and an ultimate tensile strength of 474 ± 60 MPa, whereas a limited elongation to failure (3.2 ± 2.0%) was found. It may be immediately noticed that the measured mechanical properties show a considerable dispersion. Indeed, such variability and, in particular, the limited ductility are clearly related to the presence of defects (gas porosities and hot cracks) in the produced samples. Nevertheless, the observed yield strength was largely increased with respect to that of the $CoCuFeMnNiTi_{0.13}$ alloy, produced by conventional casting and plastic deformation (269 ± 3 MPa in solution-treated condition [23]). Such improvement shall be ascribed to the refined microstructure arising from the rapid solidification

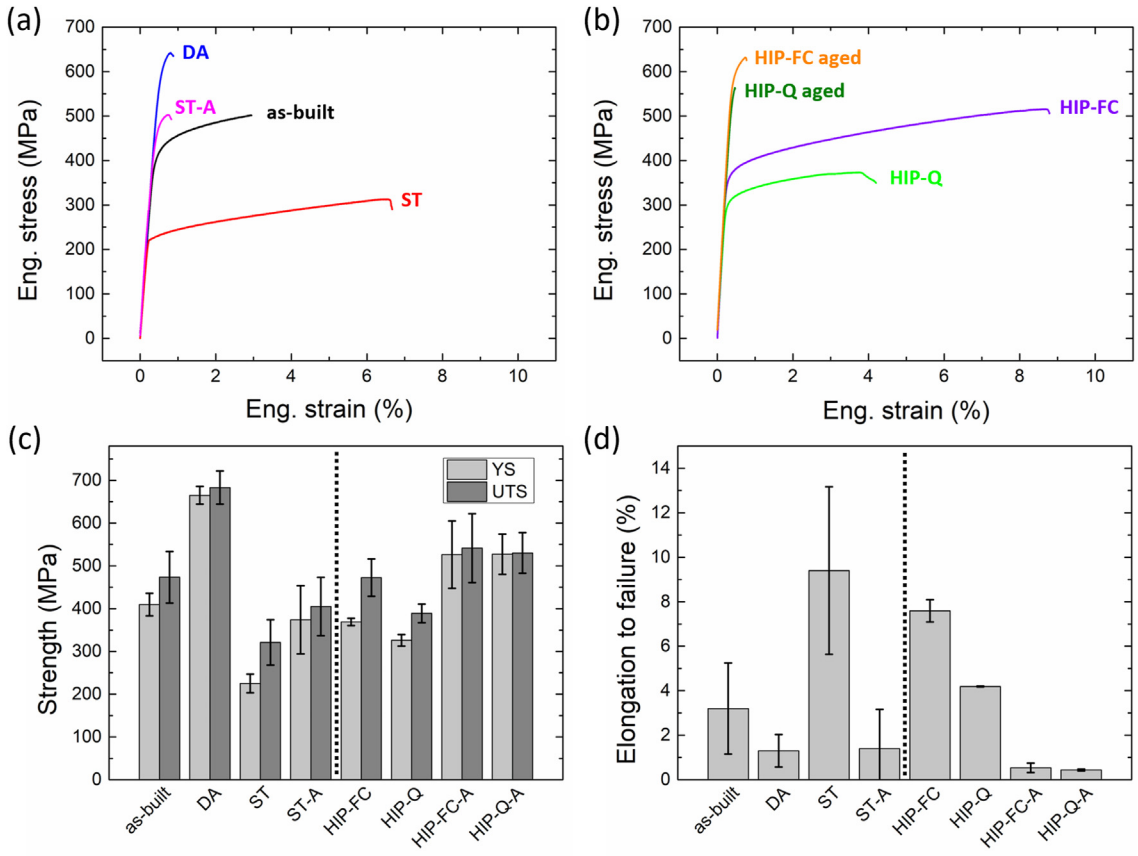


**Fig. 6 – Representative stress–strain curve of the $CoCuFeMnNiTi_{0.13}$ alloy in heat treated (a) and HIPed conditions (b); bar charts representing yield strength (YS) and ultimate tensile strength (UTS) (c) and elongation to failure (d) of the tested specimens.**

taking place during the LPBF process, to the intercalation of Cu-rich and Cu-poor FCC phases related to the dendritic microstructure and, probably, to the presence of residual stresses deriving from the layer-by layer building strategy. Post-processing thermal treatments had a strong influence on the mechanical behaviour of the alloy. Solution treatment caused an evident decrease of both yield and ultimate tensile strength, whereas elongation to failure was improved. A remarkable strength increase was induced by the ageing treatment, both in ST-A and DA conditions, but the expectable reduction in ductility related to the microstructural evolution led to average elongation to failure values as low as 1.3% and 1.7%. The tensile curves of the HIPed specimens are shown in Fig. 6 b. The reduction of defects induced by HIP led to a strong improvement in alloy ductility and to a reduction of the dispersion of elongation to failure values, as visible from the histogram of Fig. 6 d. The HIP-FC samples displayed higher strength compared to the HIP-Q specimens thanks to the slower cooling rate experienced, which was able to partially trigger spinodal decomposition and, likely, precipitation of $Ni_3Ti$. Nevertheless, both HIP-FC and HIP-Q samples present lower yield and ultimate tensile strength with respect to as-built ones: such trend may be ascribed to the disappearance of the dendritic microstructure. Similarly to what was previously observed in SìDA and ST-A samples, the application of ageing treatment to HIPed samples resulted again in a strong increase of resistance associated to an unacceptable depression of ductility. It is worth mentioning that ageing caused a 12.7% decrease of elongation to failure in the conventionally produced $CoCuFeMnNiTi_{0.13}$ alloy [23]. Thus, considering that a similar decrement may be induced in the present conditions and that the maximum achieved elongation was 13.7% (in a ST sample), it appears reasonable that all aged samples presented extremely low elongation values. Moreover, the ageing treatment apparently caused a limited decrease of density in both HIP-FC (−0.46%) and HIP-Q (−0.19%) samples and an increase in the dispersion of such density values: this suggests that some of the pre-existing and healed defects may re-open during holding at the ageing temperature.

The appearance of fracture surfaces was finally explored to better understand the ductility variations observed during tensile tests. In this light, samples, which displayed elongation to failure values at the high end of the observed variability range, were chosen; it shall nevertheless be considered that the amount and distribution of defects (pores and cracks) played a dominant role in determining the outcome of mechanical testing. It may be observed in Fig. 7 that three main different fracture modes exist throughout the studied conditions: interdendritic fracture (as-built and DA samples), ductile transgranular fracture (ST samples) and brittle intergranular fracture (ST-A, HIP-FC aged, HIP-Q aged); finally, HIP-FC and HIP-Q samples present a mixed ductile transgranular – brittle

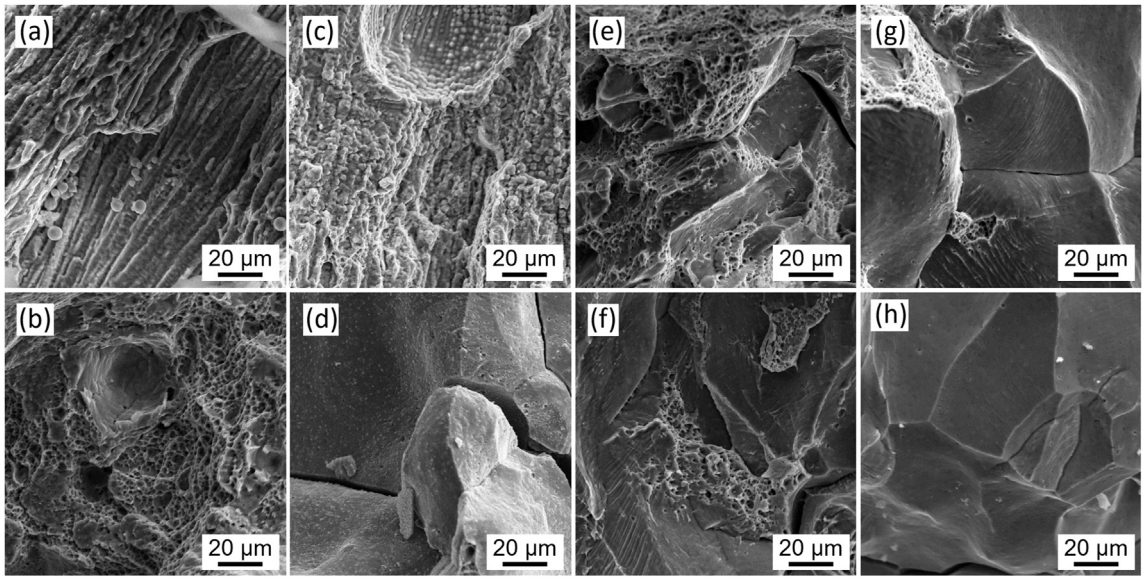


**Fig. 7 – SEM images depicting the fracture surfaces of tensile-tested $CoCuFeMnNiTi_{0.13}$ alloy in (a) as-built, (b) ST, (c) DA, (d) ST-A, (e) HIP-FC, (f) HIP-Q, (g) HIP-FC aged, (h) HIP-Q aged conditions.**

intergranular failure mode. As-built and DA samples present the typical appearance of interdendritic fracture [38]: such failure mode may be caused by the Cu-rich interdendritic phase, which has been previously described as softer than the matrix and may therefore lead to a localisation of deformation. When taking place along grain boundaries, interdendritic fracture is likely aided by the propagation of the pre-existing liquation cracks, which were described in Section 3.1. In solution-treated samples, a complete shift to a transgranular ductile fracture may be appreciated: the surface presents numerous dimples in the micrometre order, which are the result of the high elongation to failure reached by some ST samples. The following ageing treatment caused a distinct embrittlement of the alloy, leading to the activation of intergranular cracking, as made evident by the absence of dimples and the jagged appearance of the fracture surface. A similar, although less well-defined trend, holds in HIPed samples: HIP-FC and HIP-Q conditions. Such samples, which are characterised by considerable ductility, present a mixed fracture mode that is characterised by dimpled areas and intergranular cracking. On the other hand, similarly to what occurred in the non-HIPed samples, ageing treatment caused a complete transition to intergranular cracking. Such type of failure mode was also observed in the equiatomic, solution treated CoCuFeMnNi alloy after fatigue testing and was attributed to the concentration of geometrically necessary dislocations in the proximity of grain boundaries [39,40].

In essence, the present results show that only HIP treatments could produce reliable samples, characterised by a sufficient repeatability of results (Fig. 6 d). In particular, HIP-FC condition is characterised by the most balanced set of properties: the pressure applied at high temperature reduced the number of internal defects thus strongly improving the material ductility; concurrently, the relatively slow cooling allowed atomic rearrangement enabling the decomposition of the supersaturated solid solution into the Cu-containing maze-like structure and $Ni_3Ti$ precipitates.

## 4. Conclusions

Gas-atomized $CoCuFeMnNiTi_{0.13}$ HEA powder was processed by laser powder bed fusion: process optimisation led to a satisfactory densification but could not avoid the formation of hot cracks, likely caused by the liquation of the inter-dendritic Cu-rich phase. The as-built microstructure consists of columnar grains, which contain a fine dendritic structure produced by the separation of two Cu-poor and Cu-rich FCC phases upon solidification. The resulting mechanical behaviour is characterised by a good yield strength (410 MPa) and a limited ductility (elongation to failure of 3.2%) related to the present defects. The alloy responds positively to both direct ageing and solution treatment followed by ageing, showing that the spinodal decomposition and precipitation processes underlying the observed hardening are only very limitedly affected by the rapid solidification typical of LPBF. In particular, direct ageing can induce a 62% increase of yield strength with respect to the as-built condition, while the lower strength observed in solution treated and aged samples (374 MPa) should be ascribed to their high brittlness.

HIP was extremely effective in healing both pores and cracks (density was increased from 94.0% to 99.8%) and the different cooling speeds applied at the end of the treatment allowed to tailor the resulting microstructure. A high cooling rate was able to partially trigger the spinodal decomposition process during cooling, giving rise to a relatively balanced set of mechanical properties. As a result, the most balanced set of properties characterises HIPed and fast-cooled samples, which present a yield strength of 369 MPa and a repeatable elongation to failure of 7.6%.

The present work shows that on the one hand the composition of HEAs needs to be carefully tailored on the needs of the LPBF process, on the other hand post-processing treatments such as HIP and thermal treatments can be extremely effective in tailoring the microstructure of such complex alloys.

## Declaration of Competing Interest

The authors declare that they have no known competing financial interests or personal relationships that could have appeared to influence the work reported in this paper.

## Acknowledgements

The authors would like to acknowledge Sharebot (Italy) for providing the MetalOne LPBF system and for the technical assistance and Quintus Technologies (Sweden) for performing the HIP treatment. The authors also acknowledge Nicola Bennato and Enrico Bassani from CNR ICMATE, Ludovica Rovatti and Rasheed Michael Ishola from Politecnico di Milano for technical support.

## Appendix A. Supplementary data

Supplementary data to this article can be found online at https://doi.org/10.1016/j.jmrt.2023.09.223.

## REFERENCES

[1] Cantor B. Multicomponent high-entropy Cantor alloys. Prog Mater Sci 2020:100754. https://doi.org/10.1016/j.pmatsci.2020.100754.
[2] Chen S, Tong Y, Liaw PK. Additive manufacturing of high-entropy alloys: a review. Entropy 2018;20. https://doi.org/10.3390/e20120937.
[3] Jiang M, Mukherjee T, Du Y, DebRoy T. Superior printed parts using history and augmented machine learning. Comput. Mater. 2022;8. https://doi.org/10.1038/s41524-022-00866-9.
[4] Mukherjee T, Elmer J, Wei H, Lienert T, Zhang W, Kou S, et al. Control of grain structure, phases, and defects in additive manufacturing of high-performance metallic components. Prog Mater Sci 2023;138. https://doi.org/10.1016/j.pmatsci.2023.101153.
[5] Sharma A, Yadav S, Biswas K, Basu B. High-entropy alloys and metallic nanocomposites: processing challenges, microstructure development and property enhancement. Mater. Sci. Eng. R 2018;131:1–42. https://doi.org/10.1016/j.mser.2018.04.003.
[6] Liu Z, Guo S, Liu X, Ye J, Yang Y, Wng X-L, et al. Micromechanical characterization of casting-induced inhomogeneity in an Al0.8CoCrCuFeNi high-entropy alloy. Scripta Mater 2011;64:868–71. https://doi.org/10.1016/j.scriptamat.2011.01.020.
[7] Han T, Chen J, Wei Z, Qu N, Liu Y, Yang D, et al. Effect of cooling rate on microstructure and mechanical properties of AlCrFe2Ni2 medium entropy alloy fabricated by laser powder bed fusion. J Mater Res Technol 2023;25:4063–73. https://doi.org/10.1016/j.jmrt.2023.06.241.
[8] Ostovari Moghaddam A, Shaburova NA, Samodurova MN, Abdollahzadeh A, Trofimov EA. Additive manufacturing of high entropy alloys: a practical review. J Mater Sci Technol 2021;77:131–62. https://doi.org/10.1016/j.jmst.2020.11.029.
[9] Ron T, Leon A, Popov V, Strokin E, Eliezer D, Shirizly A, et al. Synthesis of refractory high-entropy alloy WTaMoNbV by powder bed fusion process using mixed elemental alloying powder. Materials 2022;15:4043. https://doi.org/10.3390/ma15124043.
[10] Xu Z, Zhang H, Li W, Mao A, Wang L, Song G, et al. Microstructure and nanoindentation creep behavior of CoCrFeMnNi high-entropy alloy fabricated by selective laser melting. Addit Manuf 2019;28:766–71. https://doi.org/10.1016/j.addma.2019.06.012.
[11] Zhang C, Feng K, Kokawa H, Han B, Li Z. Cracking mechanism and mechanical properties of selective laser melted CoCrFeMnNi high entropy alloy using different scanning strategies. Mater Sci Eng 2020;789:139672. https://doi.org/10.1016/j.msea.2020.139672.
[12] Zhang C, Feng K, Kokawa H, Li Z. Correlation between microstructural heterogeneity and anisotropy of mechanical properties of laser powder bed fused CoCrFeMnNi high entropy alloy. Mater Sci Eng 2022;855:143920. https://doi.org/10.1016/j.msea.2022.143920.
[13] Kim Y-K, Choe J, Lee K-A. Selective laser melted equiatomic CoCrFeMnNi high-entropy alloy: microstructure, anisotropic mechanical response, and multiple strengthening mechanism. J Alloys Compd 2019;805:680–91. https://doi.org/10.1016/j.jallcom.2019.07.106.
[14] Jkarlsson D, Marshal A, Johansson F, Schuisky M, Sahlberg M, Schneider J, et al. Elemental segregation in an AlCoCrFeNi high-entropy alloy - a comparison between selective laser melting and induction melting. J Alloys Compd 2019;784:195–203. https://doi.org/10.1016/j.jallcom.2018.12.2670.
[15] Wang S, Li Y, Zhang D, Yang Y, Marwana Manladan S, Luo Z. Microstructure and mechanical properties of high strength AlCoCrFeNi2.1 eutectic high entropy alloy prepared by selective laser melting (SLM). Mater Lett 2022;310:131511. https://doi.org/10.1016/j.matlet.2021.131511.
[16] Han T, Liu Y, Yang D, Qu N, Liao M, Lai Z, et al. Effect of annealing on microstructure and mechanical properties of AlCrFe2Ni2 medium entropy alloy fabricated by laser powder bed fusion additive manufacturing. Mater Sci Eng 2022;839. https://doi.org/10.1016/j.msea.2022.142868.
[17] Luo S, Gao P, Yu H, Yang J, Wang Z, Zeng X. Selective laser melting of an equiatomic AlCrCuFeNi high-entropy alloy: processability, non-equilibrium microstructure and mechanical behavior. J Alloys Compd 2019;771:387–97. https://doi.org/10.1016/j.jallcom.2018.08.290.
[18] Yang X, Heczko O, Lehtonen J, Bjorkstrand R, Salmi M, Uhlenwinkel V, et al. Microstructure and properties of additively manufactured AlCoCr0.75Cu0.5FeNi multicomponent alloy: controlling magnetic properties by laser powder bed fusion via spinodal decomposition. Materials 2022;15. https://doi.org/10.3390/ma15051801.
[19] Luo S, Zhao C, Su Y, Liu Q, Wang Z. Selective laser melting of dual phase Cocrcufeni high entropy alloys: formability, heterogeneous microstructures and deformation mechanisms. Addit Manuf 2020;31. https://doi.org/10.1016/j.addma.2019.100925.
[20] Gan G, Yang B, Zhang X, Zhu Z, Chen B, Gou G. Tuning the mechanical properties of powder bed fusion printed CoCrFeNiMn high-entropy alloys by annealing and hot isostatic pressing. J Alloys Compd 2023;946:169376. https://doi.org/10.1016/j.jallcom.2023.169376.

[21] Joseph J, Hodgson P, Jarvis T, Wu X, Stanford N, Mark D. Effect of hot isostatic pressing on the microstructure and mechanical properties of additive manufactured AlxCoCrFeNi high entropy alloys. Mater Sci Eng 2018;733:59–70. https://doi.org/10.1016/j.msea.2018.07.036.
[22] Wang X, Qiu C. Effect of aging temperature on microstructure and mechanical properties of laser melted and hot isostatically pressed (CoCrFeMnNi)96(TiAl)4 alloy. J Alloys Compd 2023;936:168317. https://doi.org/10.1016/j.jallcom.2022.168317.
[23] Fiocchi J, Coduri M, Mostaed A, Tuissi A, Casati R. Development and characterization of a novel high entropy alloy strengthened through concurrent spinodal decomposition and precipitation. J Alloys Compd 2023;947:169706. https://doi.org/10.1016/j.jallcom.2023.169706.
[24] Tazuddin, Gurao NP, Biswas K. In the quest of single phase multi-component multiprincipal high entropy alloys. J Alloys Compd 2017;697:434–42. https://doi.org/10.1016/j.jallcom.2016.11.383.
[25] Fiocchi J, Mostaed A, Coduri M, Tuissi A, Casati R. Enhanced cryogenic and ambient temperature mechanical properties of CoCuFeMnNi high entropy alloy through controlled heat treatment. J Alloys Compd 2022;910:164810. https://doi.org/10.1016/j.jallcom.2022.164810.
[26] Fiocchi J, Casati R, Tuissi A, Biffi C. Laser beam welding of CoCuFeMnNi high entropy alloy : processing, microstructure, and mechanical properties. Adv Eng Mater 2022:2200523. https://doi.org/10.1002/adem.202200523. 1–9.
[27] Kou S. Solidification and liquation cracking issues in welding. Jom 2003;55:37–42. https://doi.org/10.1007/s11837-003-0137-4.
[28] Martin AC, Oliveira JP, Fink C. Elemental effects on weld cracking susceptibility in AlxCoCrCuyFeNi high-entropy alloy. Metall. Mater. Trans. A Phys. Metall. Mater. Sci. 2020;51:778–87. https://doi.org/10.1007/s11661-019-05564-8.
[29] Stopyra W, Gruber K, Smolina I, Kurzynowski T, Kuźnicka B. Laser powder bed fusion of AA7075 alloy: influence of process parameters on porosity and hot cracking. Addit Manuf 2020;35. https://doi.org/10.1016/j.addma.2020.101270.
[30] Chauvet E, Kontis P, Jägle EA, Gault B, Raabe D, Tassin C, et al. Hot cracking mechanism affecting a non-weldable Ni-based superalloy produced by selective electron Beam Melting. Acta Mater 2018;142:82–94. https://doi.org/10.1016/j.actamat.2017.09.047.
[31] Xu J, Ding Y, Gao Y, Wang H, Hu Y, Zhang D. Grain refinement and crack inhibition of hard-to-weld Inconel 738 alloy by altering the scanning strategy during selective laser melting. Mater Des 2021;209:109940. https://doi.org/10.1016/j.matdes.2021.109940.
[32] Fiocchi J, Tuissi A, Biffi CA. Heat treatment of aluminium alloys produced by laser powder bed fusion: a review. Mater Des 2021;204. https://doi.org/10.1016/j.matdes.2021.109651.
[33] Agarwal R, Sonkusare R, Jha SR, Gurao NP, Biswas K, Nayan N. Understanding the deformation behavior of CoCuFeMnNi high entropy alloy by investigating mechanical properties of binary ternary and quaternary alloy subsets. Mater Des 2018;157:539–50. https://doi.org/10.1016/j.matdes.2018.07.046.
[34] Saheb N, Khalil A, Hakeem a S, Laoui T. Age hardening behavior of carbon nanotube reinforced aluminum nanocomposites. J Nano Res 2013;21:29–35. https://doi.org/10.4028/www.scientific.net/JNanoR.21.29.
[35] Tang M, Karma A. Surface modes of coherent spinodal decomposition. Phys Rev Lett 2012;108:1–5. https://doi.org/10.1103/PhysRevLett.108.265701.
[36] Li YS, Li SX, Zhang TY. Effect of dislocations on spinodal decomposition in Fe-Cr alloys. J Nucl Mater 2009;395:120–30. https://doi.org/10.1016/j.jnucmat.2009.10.042.
[37] Léonard F, Desai RC. Spinodal decomposition and dislocation lines in thin films and bulk materials. Phys Rev B Condens Matter 1998;58:8277–88. https://doi.org/10.1103/PhysRevB.58.8277.
[38] Hilaire A, Andrieu E, Wu X. High-temperature mechanical properties of alloy 718 produced by laser powder bed fusion with different processing parameters. Addit Manuf 2019;26:147–60. https://doi.org/10.1016/j.addma.2019.01.012.
[39] Bahadur F, Kumar J, Gururaj K, Yadav MK, Tan S, Pradeep KG, et al. Room temperature cyclic creep behaviour of equimolar CoCuFeMnNi high entropy alloy. Mater Sci Eng 2023;865:144587. https://doi.org/10.1016/j.msea.2023.144587.
[40] Bahadur F, Biswas K, Gurao NP. Micro-mechanisms of microstructural damage due to low cycle fatigue in CoCuFeMnNi high entropy alloy. Int J Fatig 2020;130:105258. https://doi.org/10.1016/j.ijfatigue.2019.105258.